SAND 95-0012 C
Conf-950130--6

NUMERICAL SIMULATION OF LAMINAR FLOW IN A CURVED DUCT

Amalia R. Lopez*

and

William L. Oberkampf**

Aerosciences and Fluid Dynamics Department, 1515
Sandia National Laboratories
Albuquerque, New Mexico 87185

Abstract

This paper describes numerical simulations that were performed to study laminar flow through a square duct with a 90° bend. The purpose of this work was two fold. First, an improved understanding was desired of the flow physics involved in the generation of secondary vortical flows in three-dimensions. Second, adaptive gridding techniques for structured grids in three-dimensions were investigated for the purpose of determining their utility in low Reynolds number, incompressible flows. It was also of interest to validate the commercial computer code CFD-ACE. Velocity predictions for both non-adaptive and adaptive grids are compared with experimental data. Flow visualization was used to examine the characteristics of the flow though the curved duct in order to better understand the viscous flow physics of this problem. Generally, moderate agreement with the experimental data was found but shortcomings in the experiment were demonstrated. The adaptive grids did not produce the same level of accuracy as the non-adaptive grid with a factor of four more grid points.

Introduction

Flows in curved ducts are found in a very wide range of practical applications of fluid dynamics. In manufacturing applications, curved ducts, diffusers, and nozzles for liquid and gas handling are ubiquitous. In aerodynamic flows, for example, the design of curved gas turbine intake ducts critically determines the compressor performance and stall characteristics over the range of engine thrust.

Several experiments have been conducted in ducts of square cross section, with short and long straight sections upstream of the curved portion. Of particular interest is the effect of thin boundary layers and fully-developed flow on the evolution of the secondary motion in the curved portion. Pioneering work in this area was done by Humphrey et al.[1]. Other representative experiments of this type are those of Taylor et al.[2], Chang et al.[3] and Iacovides et al.[4]. Measurements in fully-developed flow in a square duct clearly reveal that the secondary motion arises from curvature-induced pressure gradients which drive low-momentum fluid from the outer (concave) wall on to the inner (convex) wall. Strong curvature leads to the formation of longitudinal vortices that move toward the convex wall. The principal difference between developing and fully-developed flow is that, in the former, the secondary motion is weaker and confined to the boundary layers. The effects of surface curvature on turbulence are obviously present in these flows as well, but they are generally masked by those of the secondary motion. Also, the secondary motion due to the wall shear stress interacts with the much stronger pressure-driven secondary motion in the curved section, resulting in a flow that is influenced by different factors. Because of these flow complexities in a relatively simple geometry, square-duct experiments with a 90° bend have been used in computational code validation to test the numerical accuracy and turbulence models.

Significant contributions to the understanding of curved-duct flows have also been made through the solution of the Navier-Stokes equations. Again, pioneering work in the generation of laminar flow

---

* Senior Member Technical Staff, Member AIAA.

**Senior Member Technical Staff, Associate Fellow AIAA.

This work was supported by the United States Department of Energy under Contract DE-AC04-94AL85000.

solutions of the steady, three-dimensional Navier Stokes equations for square cross-sections was done by Humphrey et al.[5]. In addition, the laminar flow solutions of the Navier-Stokes equations by Ghia and Sokhey[6], Yoon et al.[7], and Rogers et al.[8] also demonstrate strong secondary flows. In both the Humphrey et al. and the Yoon et al. studies, it was shown that the calculated results were in fair agreement with measurements even though a small number of grid points were used. However, grid convergence and iterative convergence were not evaluated. In the Rogers et al. study, three different grids were used, but no quantitative study of grid convergence was conducted. Rogers et al. concluded that the calculated results were fairly close to the data with the exception of two trends. First, the formation of a second maximum in the streamwise velocity near the inner wall side occurs further upstream in the computations than in the experiment. Second, at the 90° bend station three velocity maxima occur, whereas the experimental measurements show two. Rogers et al. suggested that a small change in the Reynolds number or even a small amount of turbulent mixing could change the swirling mechanism enough to explain the difference between the computation and the experimental measurements.

Non-reacting, laminar flow problems, where the physics of the problem is well understood, provide a good validation test of a computational fluid dynamics (CFD) code. In addition, simple geometry problems, particularly in three-dimensions, make it easier to test specific elements of the code. In any careful validation study, it is critical to ensure that differences in results are not due to a lack of grid convergence. If the grid is too coarse, then the truncation errors, particularly in high gradient regions, makes it impossible to evaluate the physical models within the computer code. Therefore, it is necessary to run several numerical simulations with finer and finer grids until the solution does not change. For two-dimensional flows, a good example of grid convergence studies has been flow over a back step. This problem has been studied by many researchers, see for example Gartling[9], and CFD codes are commonly evaluated for this problem. However, it is not always practical, particularly in 3-D problems, to increase the grid size until grid convergence is achieved due to computer or fiscal limitations. Solution adaptive gridding is an alternative approach to achieving a grid converged solution without having to use an enormous number of grid points.

Adaptive grid generation is now an area of intense research activity, particularly for supersonic flow. There are numerous adaptive strategies found in the literature. Representative adaption techniques for Navier Stokes calculations are those of Huang et al.[10], Perng et al.[11], and Luong et al.[12]. In the latter study, improvements in shock resolution on coarse grids were shown by adapting to either the density, the gradient of density, or the curvature of density. For high Reynolds number problems, the variables chosen for adaption are also well known. Luong et al. pointed out that the utility of grid adaptation is more difficult to assess in incompressible, low Reynolds number flows, as the analyst normally "adapts" the initial grid in anticipation of the boundary layer. Thus, it is not clearly understood what is the best variable to adapt to for incompressible flow problems. Still, regions of separated flow and recirculation are not well anticipated, and it is in these applications that adaptive gridding holds promise for reducing the cost and increasing the accuracy of incompressible flows in complex geometries.

The primary purpose of this paper is to improve the understanding of the flow physics of laminar flow through a 90° curved duct of square cross-section. An additional purpose is to investigate adaptive structured grids for curved duct problems. Computational results are presented for a curved duct with a 90° bend and square cross-section. Velocity predictions from a commercial code, CFD-ACE, are compared with experimental data for a laminar, fully-developed flow at the inlet. In addition, grid convergence studies with and without adaption were performed in order to determine the size of grid necessary to obtain an accurate solution for this problem. Finally, extensive flow visualization is used to look at the characteristics of the flow though the curved duct in order to better understand the flow physics of this complex problem. Generally, moderate agreement with the experimental data was found, but shortcomings in the experiment were demonstrated.

Experimental Data

Several experiments[1,2,5] have been conducted for flow through curved ducts of square cross-section for the purpose of CFD code validation. In the experiment of Humphrey et al.[5], a 90° duct geometry was used as shown in Figure 1. The 40 x 40 mm duct had a inner radius of 72 mm and an outer radius of 112 mm. A straight duct of 1.8 m length (45 hydraulic diameters) was located ahead of the bend in order to produce inlet flow that was fully-developed. The bend was located in the vertical plane with a 1.2 m length (30 hydraulic diameters) of straight duct attached to its downstream end. In this experiment, the hydraulic diameter (H=40 mm) is defined as the length of a side of the square cross section. The bulk velocity (V_c) of the water at 25°C was 19.8 mm/s corresponding to Reynolds number (Re) of 790 based on the hydraulic diameter.

The Dean number of this flow was $De = Re(1/2H/R_c)^{1/2} = 368$, where R_c is the mean radius of

curvature. The *De* number is a similarity parameter for fully-developed flows in curved ducts of arbitrary but similar geometry. This number provides an indication of relative curvature effects and a value of 368 is considered to be a strong curvature case.

Measurements of the longitudinal component of the velocity were obtained with a laser-Doppler anemometer. In Reference 13, a detailed analysis was performed to quantify the error sources affecting the experimental measurements. The author determined that the combined effect of transit-time, gradient, and noise broadening had a negligible influence on the measured mean velocity, with an estimated precision of roughly ±0.5 % of the bulk velocity. Experimental reproducibility was checked by repeating traverses for mean velocity at various locations in the flow. Differences between traverses were smaller than the experimental uncertainty affecting the results from random error sources in the electronic instrumentation. Finally, selected contour plots for mean velocity in the longitudinal direction were integrated numerically to check that continuity was being preserved by the experimental data between measuring stations. The largest difference observed in mass flow rates between experimental stations was less than 3.5% of the bulk mass flow rate.

Humphrey et al.[5] presented velocity profiles for six streamwise locations: two locations ahead of the bend; and four locations in the bend. Only half profiles of the longitudinal velocity were presented for all radial stations shown. Measurements were taken, however, over the whole depth of the duct to check that the flow was symmetrical about the symmetry plane. As it was concluded that this was the case, to within experimental precision, the data on either side of the symmetry line were averaged to produce the profiles shown. Also, flow visualization was used in the experiment to identify qualitatively regions of recirculation.

Figure 1 also shows the coordinate system used to represent the experimental data. The streamwise coordinate is represented by x/H values before the bend, θ values in the bend, and x/H values after the bend. Before the bend, the x/H values are negative and decrease to zero at the start of the bend. In the bend, the θ values range from 0 degrees at the start, to 90 degrees at the end. After the bend, the x/H values are positive and increase from a value of zero. The gapwise or radial coordinate is represented by y/H values which range from 0.0 at the outer wall to 1.0 at the inner wall. Finally, the spanwise coordinate is represented by z/(H/2) and ranges from 0.0 at the center of the duct to 1.0 at the wall.

Computational Fluid Dynamics Code

The computer code used for the numerical simulations is CFD-ACE. It is commercially available from CFD Research Corp., Huntsville, Alabama. The code has been used in hundreds of numerical simulations. Over sixty validation test cases have been carefully evaluated using the code, ranging from incompressible flow to reacting, supersonic, two-phase flows.

Numerical Method

CFD-ACE is a pressure-based code that solves the three-dimensional, compressible, Favre-average Navier-Stokes equations in finite volume form. The code uses a multi-block approach with an implicit domain interface treatment which makes the solver fast and robust for complex geometry problems. The governing equations express the conservation laws of mass, momentum, and total enthalpy and can be written in Cartesian tensor form as follows:

$$\frac{\partial \rho}{\partial t} + \frac{d}{dx_j}(\rho u_j) = 0$$

$$\frac{\partial}{\partial t}(\rho u_i) + \frac{\partial}{\partial x_j}(\rho u_j u_i) = -\frac{\partial P}{\partial x_i} + \frac{\partial \tau_{ij}}{\partial x_j}$$

$$\frac{\partial}{\partial t}(\rho h_t) + \frac{\partial}{\partial x_j}(\rho u_j h_t) = \frac{\partial}{\partial x_j}(q_j) + \frac{\partial P}{\partial t} + \frac{\partial}{\partial x_j}(\tau_{ij} u_j)$$

$$\tau_{ij} = (\mu + \mu_t)\left(\frac{\partial u_i}{\partial x_j} + \frac{\partial u_j}{\partial x_i}\right) - \frac{2}{3}(\mu + \mu_t)\left(\frac{\partial u_k}{\partial x_k}\right)\delta_{ij}$$

$$q_j = (-\kappa)\frac{\partial T}{\partial x_j}$$

where u_i is the i-component of the velocity, ρ is the fluid density, P is the static pressure, h_t is the total enthalpy, q_j is the j-component of the heat flux, and τ_{ij} is the stress tensor (both laminar and turbulent). For turbulent flows, the Reynolds stress tensor is closed with a choice of various turbulence models. It should be noted that body forces due to gravity and coordinate system rotation can also be included in the governing equations. However, for the curved duct problem, no gravitational forces were included.

The cartesian equations are then transformed from physical space to computational space. The resulting equations are similar to the above equations with the exception that the spacial derivatives are now with respect to the coordinates in computational space. In addition, a Jacobian transformation matrix is included in each term of the equations. The transformed equations are in general non-orthogonal coordinates which allow the use of equally spaced difference formulas.

The discretization of the differential equations is carried out using a finite-volume approach. First, the solution domain is divided into a large number of discrete volumes or "cells," where all dependent flow variables and space transformation variables are stored at their geometric center. Then the fluid dynamic equations and turbulence model equations are integrated over each control volume. The finite-volume approach is used because of its attractive capability of conserving flow quantities both locally and globally.

CFD-ACE includes several different spacial difference schemes. A first-order upwind scheme is available. This tends to be the most stable scheme, but, as is well known, it is very dispersive. Two second order schemes, a central difference scheme and a second-order upwind scheme, are also options. In addition, a unique damping scheme called the Smart scheme is included in CFD-ACE. This scheme is designed to adaptively reduce to a first-order scheme, a central difference scheme, or a second-order upwind scheme as dictated by the local variation of the flow variables. Finally, other higher-order schemes such as the Osher-Chakravarthy scheme and Roe's Superbee scheme are available. For the duct problem, the central difference scheme was used in all of the numerical simulations. The second-order upwind scheme was tested on a few of the cases but did not produce as good of results as the solutions which used the central difference scheme.

The numerical solution of the discrete equations uses a pressure-based algorithm by combining the continuity and momentum equations to form a Poisson-like equation for pressure correction. The density is determined as a function of pressure via an equation of state. For incompressible flows, the density is a constant and there is no need for an equation of state or an energy equation. As a result, this algorithm is particularly appropriate to incompressible flows, but is also applicable to compressible flows.

CFD-ACE uses an iterative, segregated solution method wherein the equation sets for each variable are solved sequentially and repeatedly until a converged solution is obtained. The equation sets are solved with either an enhanced version of Stone's solver or a conjugate gradient squared method. In addition, the SIMPLE[14] algorithm and its variants are used to ensure the proper coupling of the velocity and the pressure fields. For more information on the general mathematical formulation and numerical methods in CFD-ACE see, for example, References 15, 16, and 17.

Boundary Conditions

CFD-ACE provides the capability to specify inflow, exit, wall, and symmetry boundaries over surfaces of the calculation domain. Periodic boundary conditions can also be specified, as can body forces due to gravity and to coordinate system rotation.

Two types of inflow boundary conditions are used in CFD-ACE, a prescribed mass flux boundary and a prescribed total pressure boundary. In the duct problem, the prescribed mass flux boundary was used as the inflow condition. The inflow velocity profile was prescribed to be fully developed laminar flow in a straight square duct given by Berker[18] at a location 5 hydraulic diameters ahead of the bend.

Three types of exit boundary conditions are used in CFD-ACE, a fixed pressure boundary intended for use in incompressible problems, extrapolated conditions boundary intended for use in supersonic flows, and a combination of the two intended for use where there may be subsonic and supersonic flow across an exit boundary. In the duct problem, a fixed pressure boundary was used as the exit condition at a location 5 hydraulic diameters from the end of bend.

In order to ensure that the location of the of the exit boundary did not influence the flow in the bend, two calculations, one with a straight section 5 hydraulic diameters long and another with a straight section 10 hydraulic diameters long, was conducted. There was no difference in the velocity profiles in the bend between the two calculations. In addition, the pressure field at the 5 hydraulic diameter location was essentially constant within the plane which justifies the use of a fixed pressure boundary condition. It should be noted that the flow at the exit does not have to be uniform, nor fully developed, in order to accurately use a fixed pressure boundary condition.

At a wall boundary, the velocity normal to the boundary is set to zero. This results in no mass source for the pressure correction equation. In the duct problem, a wall boundary condition was prescribed on all four sides.

At a symmetry boundary, the velocity normal to the boundary is set to zero and for all variables the gradient normal to the boundary is set to zero. This results in no mass source for the pressure correction equation and no contribution to the source term for the other equations. Symmetry boundaries were not necessary in the duct problem since the complete geometry was used. It was necessary to test grid adaption across the entire duct because of the one-dimensional adaptive approach used in the adaption code (refer to the Section Adaptive Grid Generation).

Numerical Convergence

Iterative convergence for the curved duct simulations was determined by the residual history of each dependent variable. Residuals in CFD-ACE are calculated at every grid point and represent the

imbalance in the governing equations at each iteration. Figure 2 shows the pressure residual history for all three non-adaptive grid solutions. The residual values shown in this figure are the sum of all the residuals over every grid point in the entire grid. The pressure residuals for all three grids converged approximately 6 orders of magnitude to values below 1.0e-05. In addition, all three velocity residuals (not shown) converged approximately 7 orders to values below 1.0e-06 for the each grid simulation.

As expected, the medium grid simulation converged slower than the coarse grid simulation in Figure 2. For this reason, it was necessary to run the medium grid simulations 500 iterations longer in order to converge to the same residual value. It was thought that the fine grid solution would also converge slower than the medium grid simulation and so the fine grid simulation was run for an additional 500 iterations. However, the fine grid simulation actually converged faster than the medium grid simulation. Thus, the fine grid residual converged approximately 8 orders to a value below 1.0e-07. The reason the fine grid simulation converged faster than the medium grid simulation is possibly due to the values chosen for relaxation parameters. For each grid, there is an optimum value of relaxation parameters which will increase the convergence rate. The same value of relaxation parameters was used in all three grid simulations and it is possible that the value chosen just happened to be optimum for the fine grid. No further investigation into convergence rates was conducted.

All simulations were performed on a SUN SPARCstation 10, model 51, with sufficient RAM to process each calculation in memory. The CPU times for each grid simulation are shown in Table 1 below. These times increased by a factor of 8 since each grid contained 8 times more grid points.

Table 1:

Grid	Number of Grid Points	CPUTime /Iteration (min/iter)	Total CPUTime (min)
Coarse	10,496	0.1	100
Medium	77,841	0.85	1,275
Fine	559,081	7.5	15,000

Grid Generation

In an attempt to eliminate any numerical uncertainties in the present study, detailed grid convergence studies with non-adaptive and adaptive grids were conducted. Three non-adaptive grids and four adaptive grids were generated. The variables and the methodology used for adaption is described below.

Non-Adaptive Grids

The structured grids for the duct problem were generated using the Eglin Arbitrary Geometry ImpLicit Euler (EAGLE)[19] grid generation package. The duct geometry consisted of a straight section of 5.0 hydraulic diameters ahead of the bend and a straight duct of 5.0 hydraulic diameters after the bend. Three computational grids of various sizes were generated to ensure grid convergence. The first computational grid consisted of 41 streamwise points and 16x16 cross-sectional points for a total of 10,496 grid points. The second computational grid doubled the number of points in each direction (81x31x31) for a total of 77,841 grid points. The third and finest computational grid doubled again the number of points in each direction (161x61x61) for a total of 559,081 grid points. Figure 3 shows a cross-sectional grid of the duct with the medium 31x31 grid points. All three grids were generated with grid points clustered along the walls of the duct. The ratio of the normal spacing at the center of the duct to the spacing at the wall was 4.3 for all three grids since the grids were refined uniformly. This ratio of clustering was arbitrarily chosen to capture the velocity gradients at the wall.

The distribution of the streamwise points for the coarse grid was 11 grid points in the straight section before the bend, 21 grid points in the bend, and 11 grid points in the straight section after the bend. The same streamwise distribution ratio was also used for both the medium grid and the fine grid. For all three grids, the streamwise points in the straight section were clustered near the start of the bend since the upstream influence of bend at the inlet is small. The streamwise grid spacing ratio at inlet of the computational domain to that at the start of the bend was 4.0. The points in the bend were equally spaced. The fine grid, for example, had the streamwise points spaced every 1.5° through the bend. The points in the straight section after the bend were clustered near the end of the bend in order to preserve the vortices that developed in the bend region. The streamwise grid spacing ratio at the exit of the computational domain to that at the end of the bend was 2.3.

Adaptive Grids

In order to determine the utility of grid adaption in low Reynolds number flows, the multidimensional Self-Adaptive Grid code (SAGE)[20] was used to adapt the grid to a flow-field solution. The adaptive-grid method is based on grid-point redistribution through local error minimization. The procedure is analogous to applying tension and torsion spring forces proportional to the

local flow gradient at every grid point and finding the equilibrium position of the resulting system of grid points that minimizes the solution error. The multi-dimensional problem of grid adaption is split into a series of one-dimensional problems along the computational coordinate lines. The reduced one-dimensional problem then requires a tridiagonal solver to find the location of grid points along a given coordinate line. Multi-directional adaption is achieved by the sequential application of the method in each coordinate direction. More sophisticated grid adaption procedures are available where the grid is adapted in multiple directions at one time, for example see Reference 12.

Four different adaptive grids were generated from an non-adaptive grid solution. The most accurate solution obtained with the non-adaptive grids was the fine grid (161x61x61) solution and so a smaller size grid (161x31x31) was chosen for adaption. This grid is a combination of the medium and fine grids used above. The reason for using the same number of longitudinal points as the fine grid is that adaption only occurs within each longitudinal plane and not between planes. The same number of cross-sectional points as the medium grid were chosen to see if it was possible with adaption to produce the same accuracy as the fine grid solution.

The same adaption parameters, with the exception of the adaption variable, were used to generate all four grids. The ratio of the normal spacing at the center of the duct to the spacing at the wall was specified to be 4.0. However, since there are many parameters that effect the clustering ratio, this control is not absolute and so the actual ratio for the adaptive grids was approximately 5.0.

In SAGE, the gradient of the adaption variable is first calculated in the z-direction and then in the y-direction. Initially, adaption variables such as pressure and temperature were tested. However, the solutions with these adaptive grids did not agree very well with the experimental data or the fine grid results. Instead, velocity and vorticity were chosen as suitable adaption variables for this duct problem. To start, all three velocity components were used as the adaption variables with equal influence of each. This approach produced grids with kinks in areas with small gradients simply because of the way the code adapts. Therefore, it is best to adapt to scalar quantities rather than vector components when using a series of one-dimensional adaptions. For this reason, magnitudes of velocity and vorticity components in the plane of adaption were each used as adaption variables. For example, the velocity magnitude with two components was calculated as $\text{Velocity}(2) = \sqrt{v^2 + w^2}$. Also, the total magnitude of velocity and vorticity with all three components were each used as adaption variables. For example, the velocity magnitude with three components was calculated as $\text{Velocity}(2) = \sqrt{u^2 + v^2 + w^2}$.

In the case where velocity is the adaption variable, SAGE is actually adapting to the first derivative of velocity. In the case where vorticity is the adaption variable, SAGE is actually adapting to the second derivative of velocity since vorticity is simply a combination of first derivatives of velocity. The right side of Figure 4 shows an adaptive grid at the $\theta = 90°$ plane produced by adapting to the gradient of total velocity. The left side of Figure 4 shows contours of total velocity magnitude. The adaptive grids using the three other adaption variables produced similar grids to the grid shown in Figure 4.

Discussions of Results

Velocity predictions are compared with experimental data for fully-developed laminar flow at a Reynolds number of 790. Three computational grids of various sizes were generated to ensure grid convergence. Comparisons with data of the numerical predictions for all three grids are shown at four locations in the curved portion of the duct. Results are also discussed for various adaptive grid strategies and compared with the fine grid solutions. Finally, three-dimensional flow visualization of the flow patterns in the duct are discussed.

Non-Adaptive Grid

Figure 5 shows a comparison of the numerical results for each grid with the experimental data of Humphrey et al.[5] at a streamwise location at the start of the bend, $\theta = 0°$. The variation of the streamwise component of velocity (u/Vc) in the radial direction (y/H) is shown at two spanwise locations (z/H/2). This velocity is normalized by the bulk velocity V_c. The first location (z/H/2=0.0), Figure 5a, is at the symmetry plane and the second location (z/H/2=0.5), Figure 5b, is halfway between a side wall and the symmetry plane. The numerical predictions agree well with the data at the plane of symmetry, but disagreement is noted at the intermediate plane. As can be seen, there is very little difference in the numerical results due to grid size. Even at the beginning of the bend, the influence of the bend has already caused asymmetries to appear in velocity profile.

Figure 6 shows a comparison of the numerical results with the experimental data at a streamwise location of $\theta = 30°$. The variation of the streamwise component of velocity in the radial direction is shown at two spanwise locations. Again, there is very little difference between the three numerical predictions. There are, however, notable differences between the predictions and the data.

Figure 7 shows a comparison of the numerical results with the experimental data at a streamwise location of

$\theta = 60°$. The variation of the streamwise component of velocity in the radial direction is shown at two spanwise locations. At this angular location in the bend, there is a larger difference between the three numerical results. The medium grid solution follows the fine grid solution fairly closely, while the coarse grid solution shows a much larger difference. All of the numerical predictions show large differences compared to the experimental data. In both figures, the numerical predictions show a distinct second maximum in the velocity near the inner wall. The experimental data appears to lag the numerical predictions in the streamwise development of this feature.

Figure 8 shows a comparison of the numerical results with the experimental data at $\theta = 90°$ for two spanwise locations. Both the medium and the fine grid solutions show the existence of a third maximum in the streamwise velocity near the wall. The coarse grid solution and the experimental data do not show this feature.

In order to try and resolve this troublesome difference between our predictions and the experimental data, a rough assessment of the quality of the experimental data was attempted. The mass flow rate was calculated from the velocity profiles reported at each streamwise station. A variation in the mass flow rate was noted between the stations, with a maximum difference of approximately 6% between the x/H=-5.0 location and the $\theta = 0°$ location. A similar check was made in the experiment[5] and a maximum difference of 3.5% of the bulk mass flow rate was reported. Our computation of the mass flow rate used five radial positions per measuring station as given in the report. Several more profiles, however, were measured at each station. These additional profiles could help reduce the discrepancy in the experimental mass flow rate from our check as compared to Reference 5. How a 3.5%, or 6%, error in mass flow rate might effect the velocity profiles cannot be estimated. Difficulties associated with the experimental data would only be speculation at this time.

Rogers et al.[8] also made comparisons of their numerical predictions with the same experimental data. They also used three different grids sizes. The finest grid used in that study was 121x41x41 which is in between the present medium grid and fine grid. The numerical predictions of Rogers et al. were in good agreement with the current fine grid predictions. The same two trends that were noted in the current study were also shown in Reference 8. First, the formation of the second maximum in the velocity on the inner wall side occurred further upstream in the computations than in the experiment. Second, at the 90° bend station three velocity maxima occur, whereas the experimental measurements show only two. The good agreement between two completely independent numerical formulations and computer codes lends significant credence to the accuracy of these predictions. For the present case of steady laminar incompressible flow, high quality CFD solutions should yield accurate solutions to the Navier Stokes equations.

Adaptive Grid

Four different adaptive grid strategies were developed and applied using the SAGE code. As discussed in the Section Adaptive Grid Generation, velocity and vorticity were chosen as the best adaption variables for this incompressible flow problem. The magnitude of velocity and vorticity in the plane of adaption were each used as adaption variables. The total magnitude of velocity and vorticity (including all three components) were also used as adaption variables. The SAGE code was used to adapt to the gradient of these variables in each direction of the planes across the duct.

Figure 9 shows a comparison of the numerical results for the fine grid and for the four adaptive grids at a streamwise location of $\theta = 30°$. The streamwise component of velocity is shown at the same two spanwise locations discussed earlier. The numerical predictions generated with adaptive grids were almost identical to the fine grid solution. However, the adaptive grid solution which used two components of velocity (Velocity(2)) did differ slightly from the fine grid solution. The grid used to generate this solution was the most distorted of all the adaptive grids and, apparently, failed to locate points in the regions with the largest truncation errors.

Figure 10 shows a comparison of the numerical results for the fine grid and the four adaptive grids at a streamwise location of $\theta = 60°$. At this location, there is a noticeable difference between the adaptive grid predictions and the fine grid solution. Again, the Velocity(2) adaptive grid solution shows the largest difference. In Figure 10a, the adaptive grid solutions capture the first and second maximum in velocity quite well, but are higher than the fine grid solution in the minimum velocity region. In Figure 10b, the adaptive grid solutions capture the maximum in velocity near the outer wall, but fail to capture the maximum near the inner wall as well as the fine grid solution.

Figure 11 shows a comparison of the numerical results for the fine grid and the four adaptive grids at a streamwise location of $\theta = 90°$. Again, there is a noticeable difference between the adaptive grid predictions and the fine grid solution with the Velocity(2) adaptive grid solution differing the most. In Figure 11a, the adaptive grid solutions capture the velocity maximum near the inner and outer walls, but

none capture the velocity maximum near y/H=0.35. In Figure 11b, the adaptive grids yield similar results; near the walls they capture the flow features, but in the interior of the duct they do not produce accurate solutions.

Overall, the grids adapted to the total magnitude of either velocity or vorticity produced the best results but they still failed to capture all of the features shown in the fine grid solution. In general, it did not appear to make a big difference in the solution whether the grids were adapted to the first or second derivatives of velocity. The grid adapted to vorticity using two components produced results that were similar to those using three components. The grid adapted to velocity using two components produced results which were in poorest agreement with the fine grid results.

Recall that the objective for using adaptive grids was to reduce the number of grid points necessary to obtain an accurate solution. As discussed above, the numerical predictions using adaptive grids failed to produce the same accuracy as the fine grid solution with a four times more grid points. A much less demanding question was also asked: Did the adaptive grids produce better results than the non-adaptive medium grid? Figure 12 compares the adaptive grid solution with the non-adaptive medium and fine grid solutions at the 90° station. In this figure, the Voriticity(3) adaptive grid solution is used as representative of all adaptive grid solutions. From comparing the non-adaptive medium grid solution to the adaptive medium grid solution, there was essentially no improvement in solution quality obtained from grid adaption. Possibly a better set of adaption variables could be found which would produce improved results from those given here. However, our investigation argues that adaptive gridding for this incompressible, low Reynolds number flow is of minimal value added for the effort expended.

Flow Physics

Figure 13 shows cross-sections of the duct at four spanwise locations of $\theta = 0^\circ, 30^\circ, 60^\circ, 90^\circ$. The left side of Figure 13 shows the velocity magnitude contours and the right side shows velocity vectors from the fine grid results. The velocity contour plots show how the high-velocity fluid accumulates very close to the outside wall at the end of the 90° turn. These plots also shows the formation of the vortices that bring some of this high-velocity fluid toward the inner wall, forming the second maximum in the velocity near the inside wall at about the 60° location. At the 90° location, the induced vortical flow has wrapped the region of higher velocity fluid toward the middle, which causes the third maximum in velocity as seen in Figure 8.

The cross-stream velocity vectors also shown in Figure 13 clearly show the vortical motion caused by the bend. At the 0° location, it is clear that the mean flow has already been influenced by the downstream flow. By the 30° location, one pair of vortices has been generated on the outside wall. The center of the vortices moves towards the inside wall between the 30° and 60° locations. At the 90° location, the vortices appear to have moved somewhat away from the inner wall, and at the same time another pair of vortices have developed near the outside wall. These results qualitatively agree with the observations in the experiment of Humphrey et al.[5] and the numerical results of Rogers et al[8].

Figure 14 shows contours of wall static pressure in the duct. It is seen that the peak pressure occurs on the outer wall near the end of the turn. This curvature-induced pressure gradient causes secondary motion to develop and longitudinal vortices to form. In addition, the unfavorable pressure gradient along the outer wall is large enough to produce a region of separated flow near the outer wall.

Figure 15 shows streamline patterns along the symmetry plane. These patterns show the fluid moving from the inner wall to the outer wall. Whereas, in Figure 16, the streamline patterns along a side wall show the fluid moving from the outer wall to the inner wall. The direction of flow along the walls depends almost entirely on pressure; whereas, the direction of flow in the plane of symmetry depends on a combination of both pressure and momentum. Also shown in Figure 16 is the reverse flow region which develops along the outer wall. It appears, from this figure, that the reverse flow region starts just ahead of the 0° location. In the Humphrey et al. experiment[5], the separated flow region was observed between 0° and 25°. However, it is impossible to quantitatively determine from the dye traces in the detailed report[13] exactly where the separated flow region begins and ends. In the current study, the range of flow reversal was from x/H = -0.25 to $\theta = 40.5^\circ$.

Figure 17 shows streamline patterns along the outer wall of the duct. In the bend, the streamlines clearly show the secondary motion which moves fluid away from the symmetry plane towards the side walls. This figure also shows the region of flow reversal extending inward from the side walls a small distance. Figure 18 shows streamline patterns along the inner wall. The patterns shown in this figure are the result of two sets of vortices. In the bend, the pattern is due to the largest vortices pulling fluid toward the plane of symmetry. After the bend, the pattern is a combination of this feature and that due to smaller vortices near the wall moving fluid away from the plane of symmetry. Refer to

Figure 13d for a better understanding of the flow pattern near the inner wall.

Figure 19 shows streamtubes which follow the center of the primary vortices as they move through the duct. Three cross-sectional velocity planes are included to better visualize the position of the vortices at each station. This figure clearly shows the movement of the vortices from the outer wall to the inner wall. It also shows how they move from near the side walls toward the plane of symmetry. They persist and are seen to exit the view of this figure at x/H=+5.0.

Figure 20 shows both the radial (y/H) and the spanwise (z/(H/2)) locations of the center of vortices as a function of the streamwise (θ) coordinate through the bend. The vortices start to develop after the 0° location but it is difficult to determine the center of the vortices before the 7.5° location. In the radial direction, the center of the vortices are closer to the outer wall near the start of the bend and move towards the inside wall between the 30° and 60° location as seen in Figure 13. In the spanwise direction, the center of the vortices are closer to the side wall and eventually move to a location midway between the symmetry plane and the side wall. The radial and spanwise locations of the primary vortices provides quantitative results from the present computational results so that other CFD validation results can be compared to ours.

Conclusions

Computational predictions were compared with experimental data obtained by Humphrey et al.[5] for fully-developed laminar flow at a Reynolds number of 790. Moderate agreement with the experimental data was found, but troublesome differences were identified. The present results were in good agreement with previous computational results of Rogers et al.[8] Good agreement between two completely independent numerical formulations and computer codes lends significant credence to the accuracy of these predictions. Difficulties associated with the experimental data would only be speculation at this time.

From numerical experiments with various grid adaption variables, it was determined that it is best to adapt to scalar quantities rather than vector components when using a series of one-dimensional adaptions. Grids adapted to the total magnitude of either velocity or vorticity produced the best results but they still failed to capture all of the features shown in the fine grid solution. In general, it did not appear to make a noticeable difference in the solution whether the grids were adapted to the first or second derivatives of velocity. Thus, it was concluded that for this low Reynolds number problem, the gradients produced by the secondary vortical flow were not very large and so adaption did not significantly improve the accuracy of the results. Possibly a better set of adaption variables could be found which would produce improved results from those given here.

Finally, flow visualization from the fine grid solutions helped to better understand the flow physics of this complex problem. Viewing the center of the vortices with streamtubes provided a better perspective to the characteristics of the flow. In addition, the locations of the primary vortices was provided so that other CFD results could be compared to our quantitative data. Other CFD researchers are encouraged to compute this flow in order to determine the correct flow field to this validation test case. The flow generated in the duct is rich in fluid physics with the development of secondary flow, longitudinal vortices, and reverse flow. For this reason, the curved duct problem appears to be a good CFD validation case of three-dimensional, laminar flow. It is recommended that experimental measurements with the laser-Doppler anemometer should be carefully redone to provide detailed experimental data for CFD validation.

Acknowledgments

The authors wish to acknowledge Jeffrey L. Payne (Aerosciences and Fluid Dynamics Dept., Sandia National Laboratories) for his help with adaptive gridding and flow visualization. The authors also wish to acknowledge Don E. Larson (Manufacturing & Environmental Fluid Dynamics Dept., Sandia National Laboratories) for his help in post-processing the numerical results. Finally, the authors wish to thank the support staff from CFD Research Corp. for very generous and prompt advice.

References

1. Humphrey, J. A. C., Whitelaw, J. H., and Yee, G., "Turbulent flow in a square duct with strong curvature," *J. of Fluid Mechanics*, Vol. 103, pp.443-463, 1981.

2. Taylor, A. M. K. P., Whitelaw, J. H., and Yianneskis, M., "Measurements of Laminar and Turbulent Flow in a Curved Duct With Thin Inlet Boundary Layers," NASA Contractor Report 3367, 1981.

3. Chang, S. M., Humphrey, J. A. C., Johnson, R. W., and Launder, B. E., "Turbulent momentum and heat transfer in flow through a 180 degree bend of square cross section," *Proc. 4th Symposium on Turbulent Shear Flows*, Karsruhe, Germany, 1983.

4. Iacovides, H., Launder, B. E., Loizou, P. A., and Zhao, H. H., "Turbulent boundary layer development around a square-sectioned U-bend: measurements and computation," *J. of Fluid Engineering*, Vol. 112, pp.

409-415, 1990.

5. Humphrey, J. A. C., Taylor, A. M. K., and Whitelaw, J. H., "Laminar flow in square duct with strong curvature," *J. of Fluid Mechanics*, Vol. 83, p. 509, 1977.

6. Ghia, K. N. and Sokhey, J. S., "Laminar incompressible viscous flow in curved ducts of regular cross sections," Trans. A.S.M.E. I, *J. of Fluid Engineering*, Vol. 99, p. 640, 1977.

7. Yoon, S., Kwak, D., and Chang, L., "LU-SGS Implicit Algorithm for Three-Dimensional Incompressible Navier Stokes Equations with Source Term," Paper No. 89-1964-CP, AIAA 9th Computational Fluid Dynamics Conf., Buffalo, NY, June, 1989.

8. Rogers, S. E., Kwak, D., and Kiris, C., "Steady and Unsteady Solutions of the Incompressible Navier-Stokes Equations," *AIAA Journal*, Vol. 29, No. 4, pp. 603-610, April, 1991.

9. Gartling. D. K., "A Test Problem for Outflow boundary Conditions - Flow Over a Backward-Facing Step," *International Journal for Numerical Methods in Fluids*, Vol. 11, pp. 953-967, 1990.

10. Huang, W. and Sloan, D. M., "A Simple Adaptive Grid Method in Two Dimensions," *Journal of Science and Computers*, Vol. 15, No. 4, pp. 776-797, July, 1994.

11. Perng, C. Y. and Street, R. L., "An Adaptive Grid Calculation for the Incompressible Unsteady Navier-Stokes Equations," Adaptive Computation Methods in Environmental Transport Processes ASME, HTD-Vol. 208, pp. 27-33, New York, 1992.

12. Luong, P. V., Thompson, J. F., and Gatlin, B., "Adaptive EAGLE: Solution-Adaptive and Quality-Enhancing Multi-Block Grids for Arbitrary Domain," Paper No. 91-1593, AIAA 10th Computational Fluid Dynamics Conf., Honolulu, HI, June, 1991.

13. Humphrey, J. A. C., "Flow in Ducts with Curvature and Roughness," Dissertation for Department of Mechanical Engineering, Imperial College of Science and Technology, London, June, 1977.

14. Patankar, S. V. and Spalding, D. B., "A Calculation Procedure for Heat, Mass and Momentum Transfer in Three-Dimensional Parabolic Flows," *Int. J. Heat Mass Transfer*, Vol. 15, pp. 1787-1806, 1972.

15. Yang, H.Q. and Przekwas, A. J., "Pressure-Based Higher Order TVD Methodology for Dynamic Stall Simulation," Paper No. 93-0680, AIAA 31st Aerospace Sciences Conf., Reno, NV, January, 1993.

16. Lai, Y. G., Przekwas A. J., and So, R. M. C., "Aerodynamic Flow Simulation Using a Pressure-Based Method and a Two Equation Turbulence Model," Paper No. 93-2902, AIAA 24th Fluid Dynamics Conf., Orlando, FL, July, 1993.

17. Jiang, Y., Lai, Y. G., Ho, S. Y, and Przekwas, A. J., "3D Simulation of Complex Flows with an Implicit Multi-Domain Approach," Paper No. 93-3124, AIAA 24th Fluid Dynamics Conf., Orlando, FL, July, 1993.

18. Berker, R., *Handbuch der Physik*, Vol. III, Pt. 2, pp.1-384, Springer, Berlin, 1963.

19. Dukowicz, J. K., "Conservative Rezoning (Remapping) of General Quadrilateral Meshes," *J. of Computational Physics*, Vol. 54., 1984.

20. Davies, C. B. and Venkatapathy, E., "The Multidimensional Self-Adaptive Grid Code, SAGE," NASA Technical Memorandum 103905, 1992.

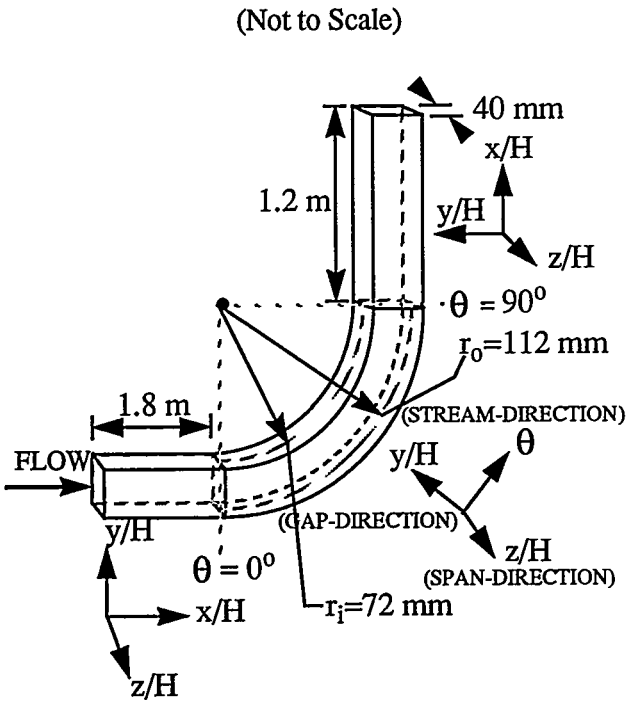

Figure 1: 90° Duct Geometry and Coordinate System

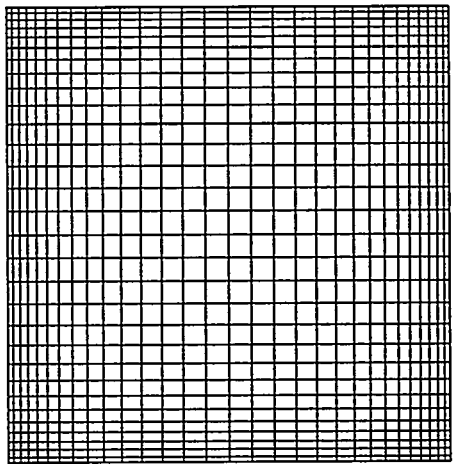

Figure 3: Medium Grid Cross-Section of Duct

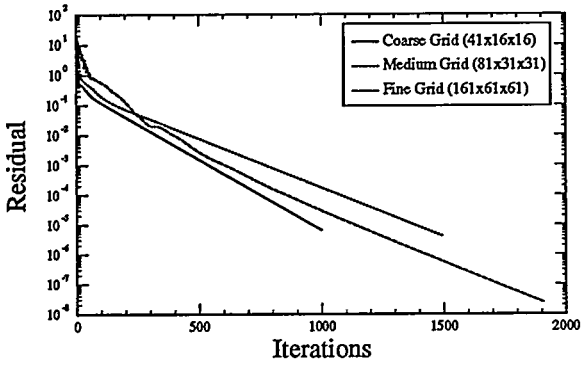

Figure 2: Pressure Residual History for Non-Adaptive Grids

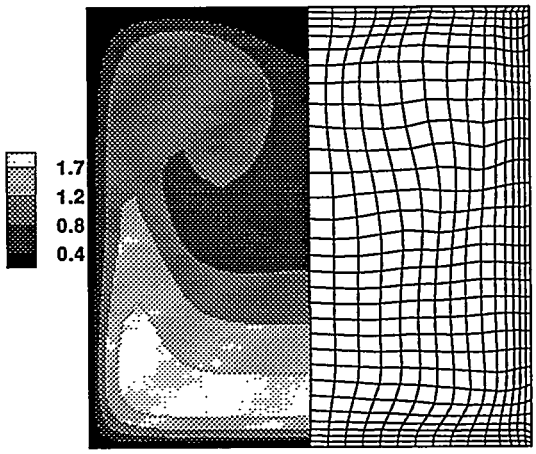

Figure 4: Total Velocity Magnitude Contours and and Corresponding Adaptive Grid

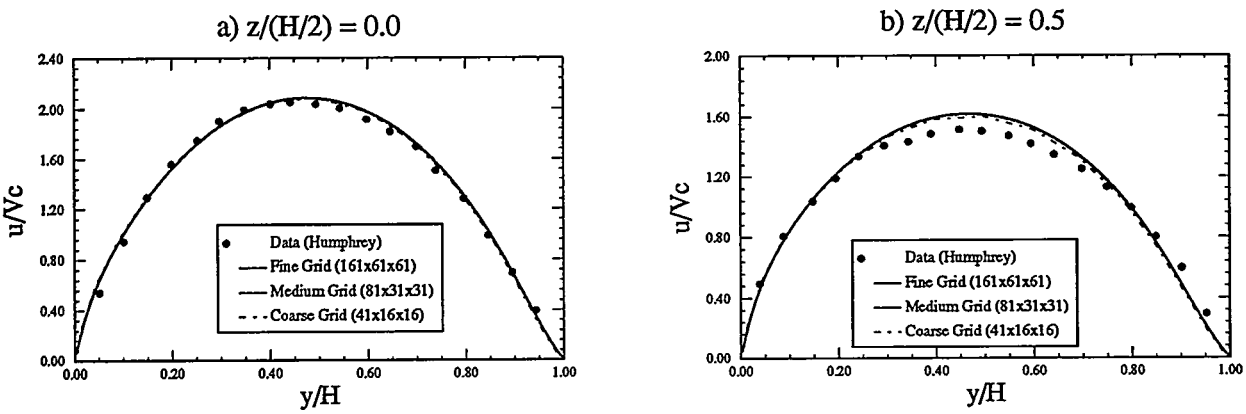

Figure 5: Radial Variation of Streamwise Velocity at $\theta = 0^{\circ}$ for Two Spanwise Locations / Non-Adaptive Grids

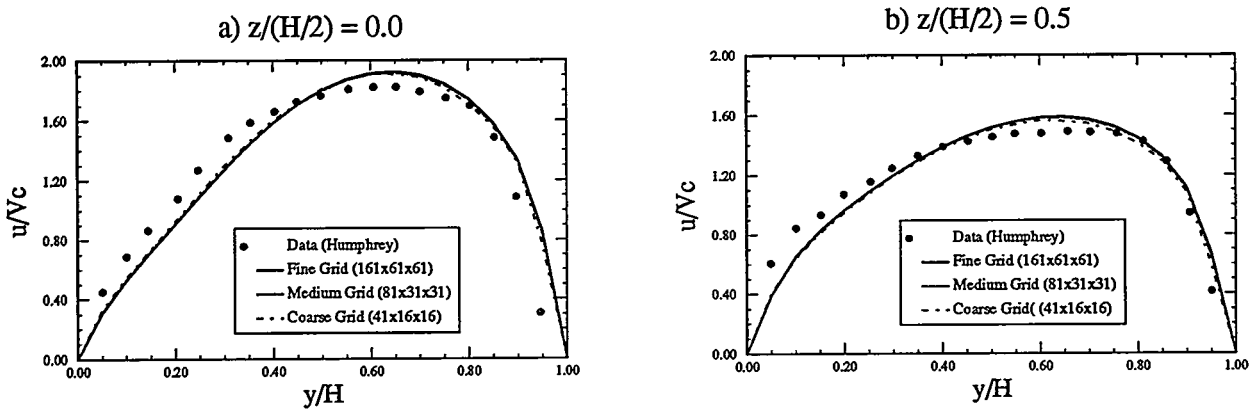

Figure 6: Radial Variation of Streamwise Velocity at $\theta = 30^{\circ}$ for Two Spanwise Locations / Non-Adaptive Grids

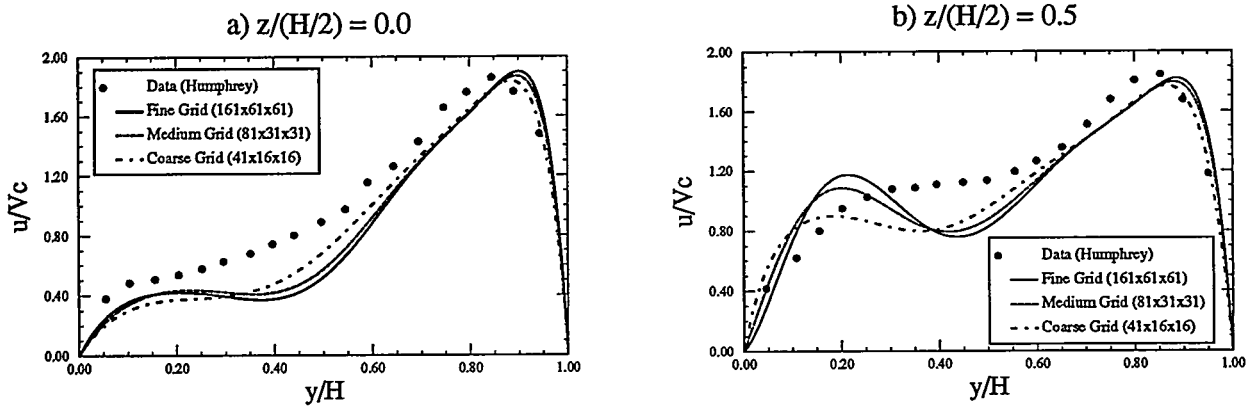

Figure 7: Radial Variation of Streamwise Velocity at $\theta = 60^{\circ}$ for Two Spanwise Locations / Non-Adaptive Grids

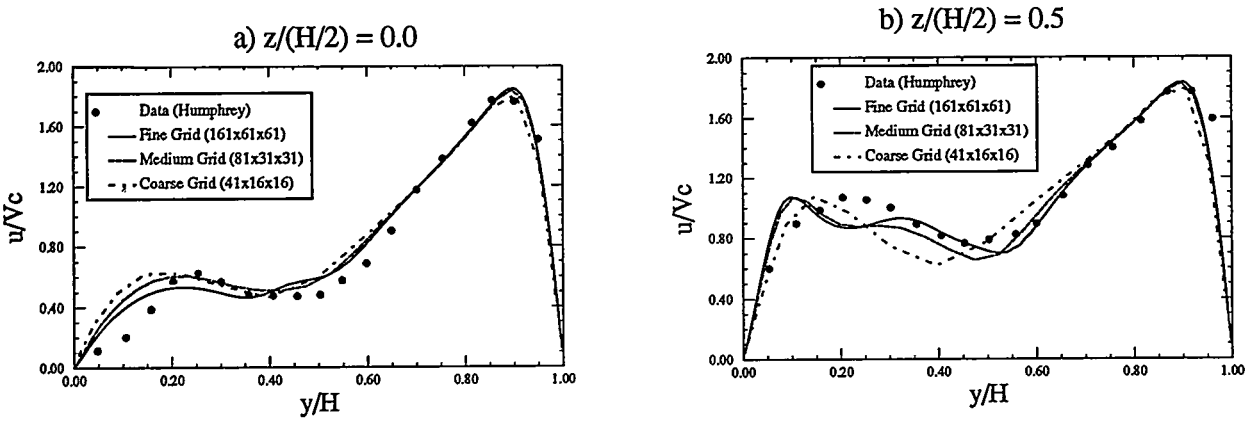

Figure 8: Radial Variation of Streamwise Velocity at $\theta = 90^{\circ}$ for Two Spanwise Locations / Non-Adaptive Grids

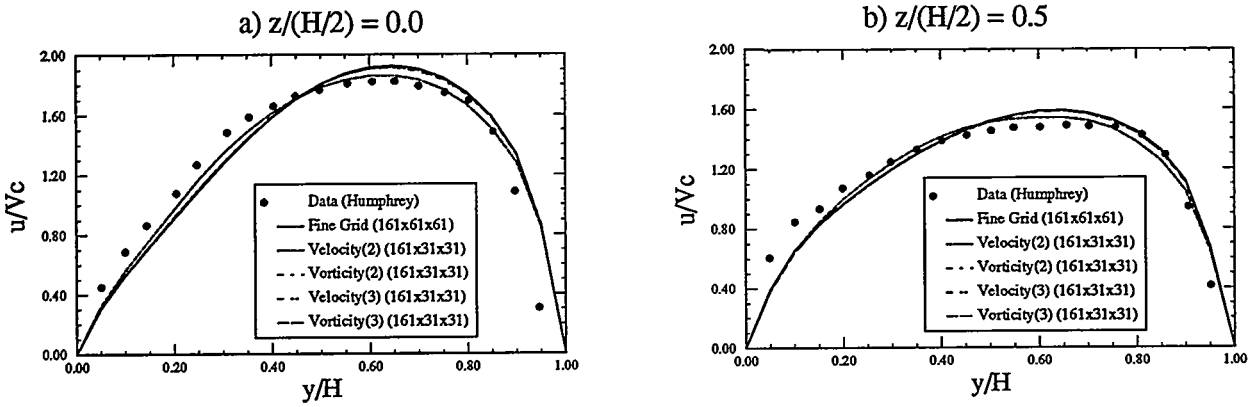

Figure 9: Radial Variation of Streamwise Velocity at $\theta = 30^{\circ}$ for Two Spanwise Locations / Adaptive Grids

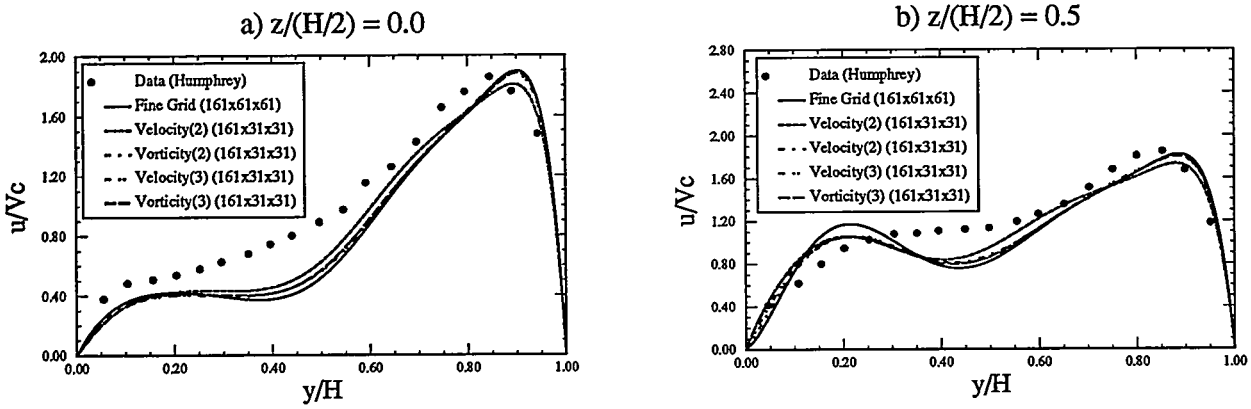

Figure 10: Radial Variation of Streamwise Velocity at $\theta = 60^{\circ}$ for Two Spanwise Locations / Adaptive Grids

a) z/(H/2) = 0.0

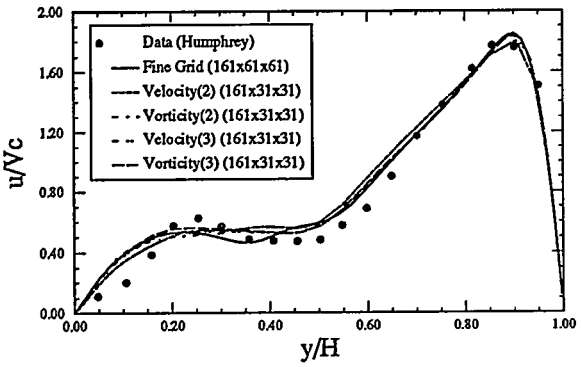

b) z/(H/2) = 0.5

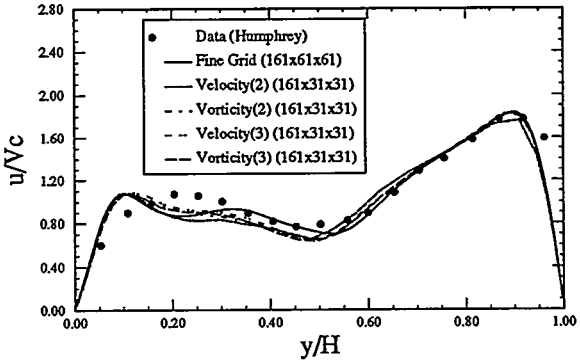

Figure 11: Radial Variation of Streamwise Velocity at $\theta = 90^{\circ}$ for two Spanwise Locations / Adaptive Grids

a) z/(H/2) = 0.0

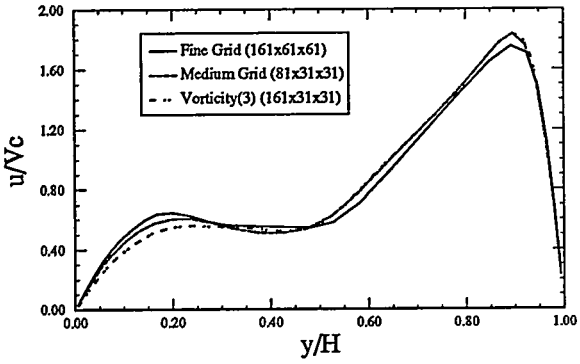

b) z/(H/2) = 0.5

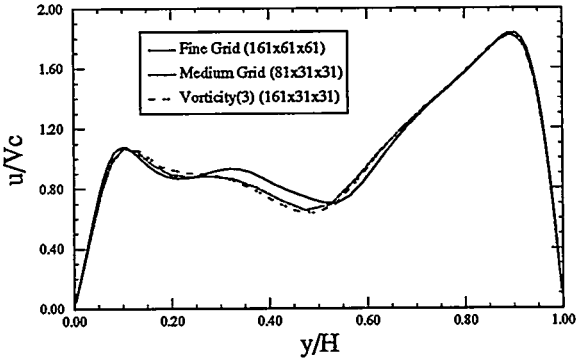

Figure 12: Radial Variation of Streamwise Velocity at $\theta = 90^{\circ}$ for two Spanwise Locations / Both Grids

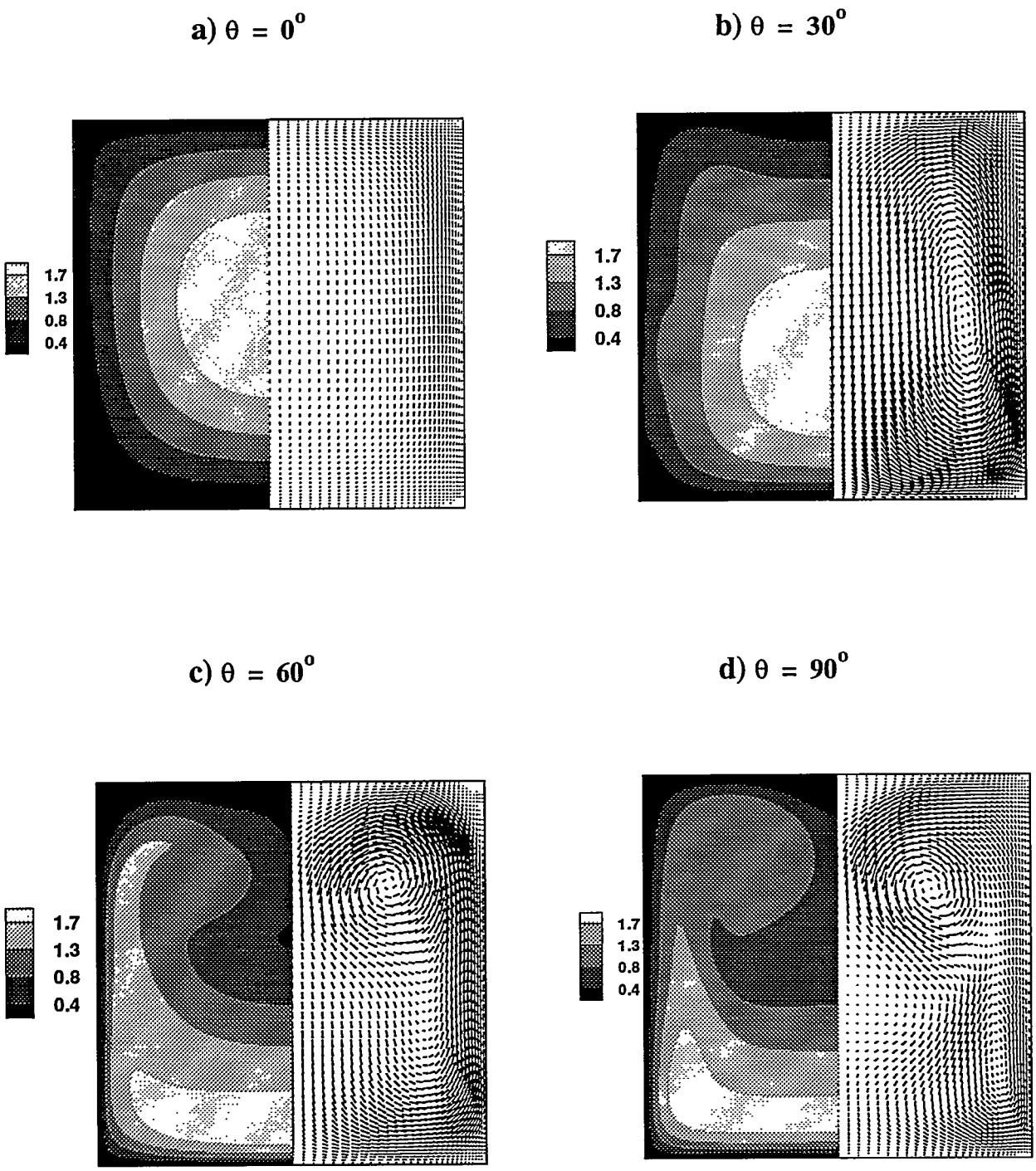

Figure 13: Velocity Magnitude Contours and Cross-Sectional Velocities at Four Streamwise Locations

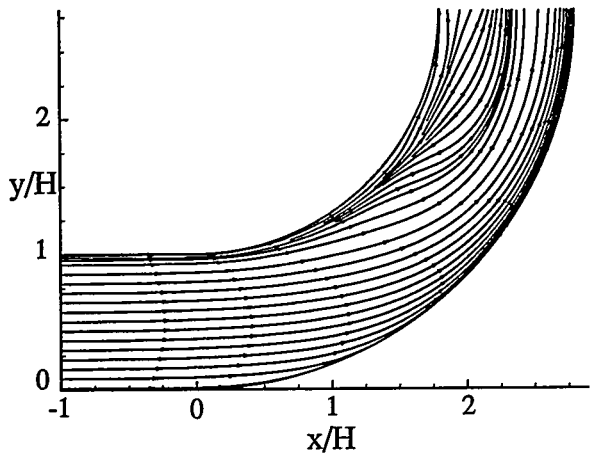

Figure 15: Streamline Patterns Along Symmetry Plane

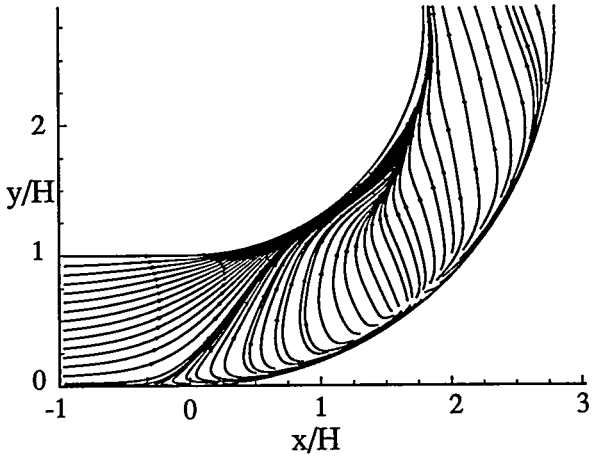

Figure 16: Streamline Patterns Along Side Wall

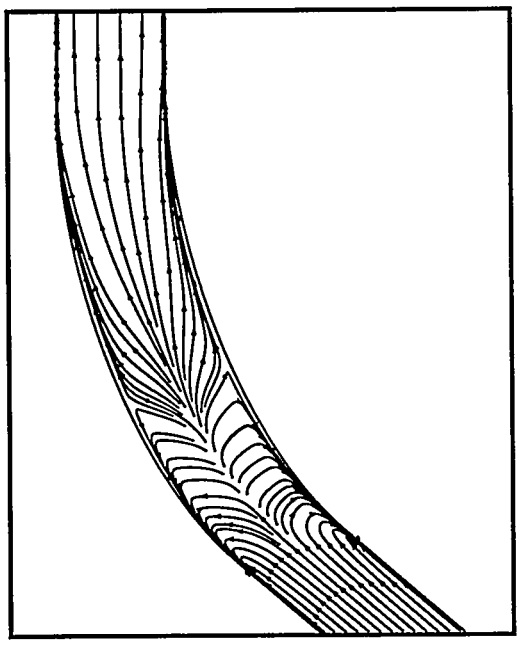

Figure 17: Streamline Patterns Along Outer Wall

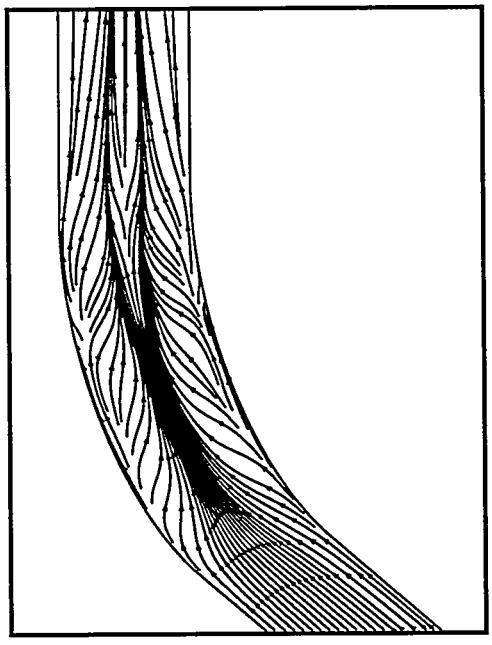

Figure 18: Streamline Patterns Along Inner Wall

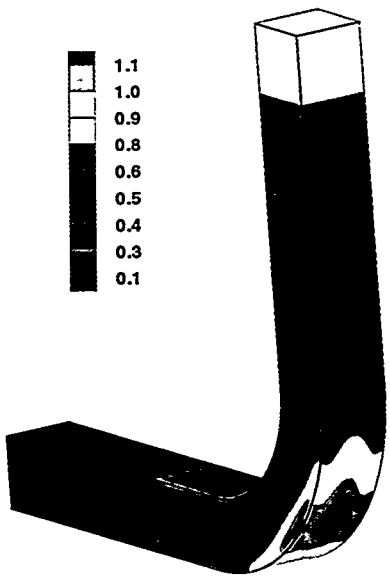

Figure 14: Surface Pressure Contours for Curved Duct

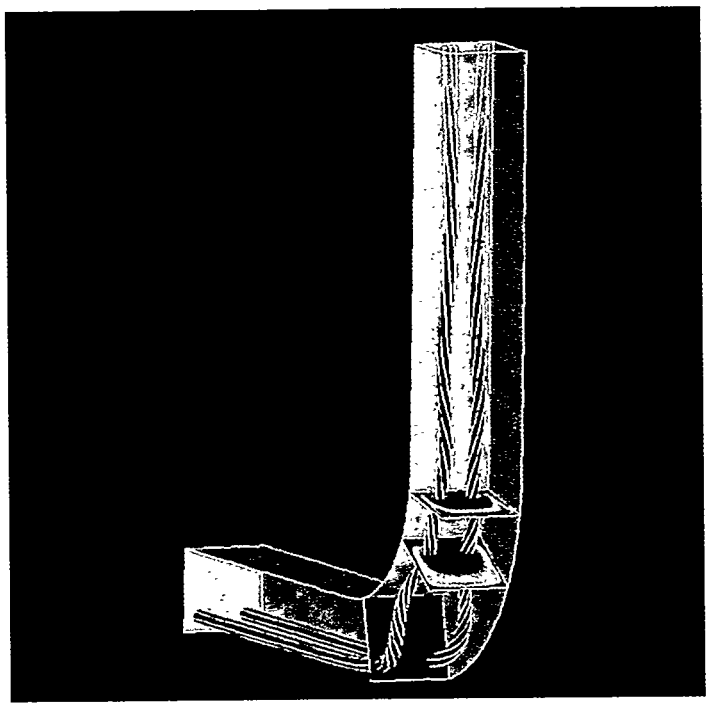

Figure 19: Streamtube Pattern of Vortex Centers in Curved Duct

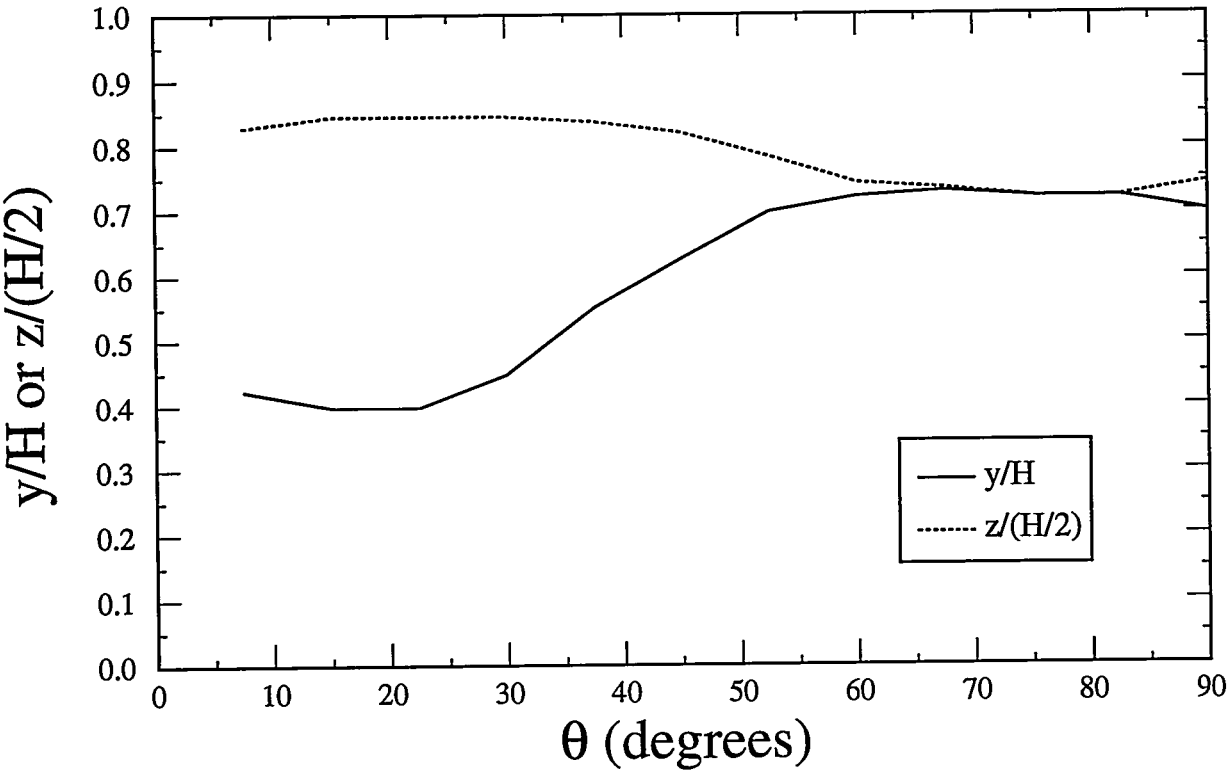

Figure 20: Streamwise Variation of Vortex Center Locations in Curved Duct